Charge Control of Critical Conduction Mode Grid-Tied Inverters to Enhance Dynamics and Robustness

Yuying He, *Member, IEEE*, Li Zhang, *Senior Member, IEEE*, Zhengzi Lei, *Student Member, IEEE*, Zhongshu Zheng, *Student Member, IEEE*, and Wenbo An, *Student Member, IEEE*

***Abstract*—Critical conduction mode (CRM) operation stands as a highly effective strategy for grid-tied inverters to achieve zero-voltage switching, thereby minimizing switching losses and circumventing the switching frequency limitation. To eliminate the additional hardware cost and complexity associated with conventional zero-crossing detection circuits, fully digital control implementations for CRM have attracted much research interest. This article introduces a novel charge control methodology. The core principle involves precisely regulating the total charge transferred through the inverter-side inductor within each well-defined control cycle. Crucially, this approach directly establishes and leverages a deterministic regulatory relationship between the commanded charge quantity and the required turn-ON time of the switches. Beyond enabling reliable CRM-based zero-voltage-switching operation, the proposed charge control inherently reduces the system order compared to traditional average current control schemes, facilitates faster dynamic response due to its the direct charge-to-time mapping mechanism and demonstrates enhanced robustness against grid impedance variations. Experimental validation conducted on a 1-kW prototype inverter operating under typical grid conditions verifies the effectiveness of the proposed control strategy in achieving these advantages.**

***Index Terms*—Charge control, critical conduction mode, dynamic response, grid-tied inverter, stability.**

I. Introduction

GRID-TIED inverters with high efficiency and quality are widely employed in Photovoltaic microinverters [1], [2], EV onboard chargers [3], and auxiliary power supply in railway applications [4]. Over the past decades, researchers have been dedicated to enhancing the efficiency and compactness of grid-tied inverters through the utilization of wide-bandgap devices, such as high-frequency silicon carbide MOSFETs [5], [6], [7], [8]. Nevertheless, due to the high turn-ON loss by hard-switching, it is still challenging to push the switching frequency up to several hundreds of kHz in the continuous conduction mode (CCM). To minimize switching losses and overcome the limitations of switching frequency, many researches are thus extensively conducted on the critical conduction mode (CRM) operation in the grid-tied inverter, where zero-voltage-switching (ZVS) can be achieved [9], [10], [11], [12].

In the realm of CRM grid-tied inverters, the average current control scheme is commonly adopted in the existing literature [13], [14], [15], [16], [17]. In [14], the average current loop is used to obtain the ON-state time of the switches, and a zero-crossing detection (ZCD) circuit with the turn-OFF extension technique is employed to regulate the OFF-time of the switches. In this way, the full-range ZVS turn-ON can be effectively achieved. However, the ZCD circuit inherently requires high-bandwidth comparators and precision current sensors, leading to increased hardware complexity and cost. In contrast, fully digital CRM control obviates the need for such high-bandwidth components, offering a more cost-effective solution. This advantage has positioned the fully digital CRM control as a subject of growing research focus.

A critical challenge arises from its variable switching frequency in CRM operation, which may range from hundreds of kilohertz to megahertz. Precisely regulating the ON-time, OFF-time, and deadtime of switches ON a per-switching-cycle basis imposes a substantial computation burden on the digital controller, limiting real-time implementation feasibility. To address this issue, Son et al. [15], [16] introduced a state-plane plot based on a constant digital control frequency to calculate the ZVS turn-ON delay. Zheng et al. [17] developed a fully digital ZVS control scheme with an optimized digital control frequency. These methods avoid the ZCD circuit and reduce the performance demands on digital controllers. Despite this improvement, the system still encounters challenges such as complex parameter design and sensitivity to grid impedance fluctuations [18], [19].

To tackle the above challenges, state-of-the-art control strategies including model predictive control (MPC) [20], [21], [22], adaptive control [23], [24], [25], and one-cycle control (OCC) [26], [27], [28], [29], [30], have garnered significant research attention. Among them, the MPC utilizes dynamic model

Received 8 February 2025; revised 17 April 2025 and 24 June 2025; accepted 23 July 2025. Date of publication 28 July 2025; date of current version 8 September 2025. This work was supported in part by the National Natural Science Foundation of China under Grant 52322705 and in part by the Natural Science Foundation of Jiangsu Province under Grant BK20230037. Recommended for publication by Associate Editor A. Davoudi. *(Corresponding author: Li Zhang.)*

The authors are with the School of Electrical and Power Engineering, Hohai University, Nanjing 211100, China (e-mail: heyuying@hhu.edu.cn; zhanglinuaa@hhu.edu.cn; hhulzz@hhu.edu.cn; hhuzzs@hhu.edu.cn; anwenbo@hhu.edu.cn).

Color versions of one or more figures in this article are available at https://doi.org/10.1109/TPEL.2025.3593141.

Digital Object Identifier 10.1109/TPEL.2025.3593141

prediction and receding-horizon optimization, which is preferable for the multivariable complex system, such as motor drives and multilevel inverters [20], [21]. Nonetheless, its practical implementation is limited due to large computation burden, inconstant switching frequency, and parameter mismatch [22]. The adaptive control, conversely, enhances system robustness through online parameter identification and dynamic controller tuning [23], [24], [25], at the cost of transient performance degradation due to delayed parameter convergence. In contrast, the OCC distinguishes itself with simple implementation, minimal computational demands, and robust stability, enabling widespread adoption in dc–dc converters [26] and rectifiers [27], [28]. Recent studies, such as composite-function-embedded OCC for expanded stable regions in buck–boost converters [29] and enhanced OCC schemes for accelerated dynamic response [30], further underscore its potential.

However, conventional OCC schemes requires fixed switching frequency, rendering them incompatible with CRM inverters characterized by time-varying switching frequencies [31], [32]. This article attempts to fill this void by extending OCC to CRM grid-tied inverters.

Beyond achieving OCC in CRM mode operation, system stability analysis and enhancement are critically important, particularly for *LCL*-type grid-tied inverters. While *LCL* filters are favored in practical applications thanks to their superior harmonic attenuation ability and compact size [33], [34], they introduce sensitivity to grid impedance fluctuation. This susceptibility can lead to destabilizing inverter-grid interaction resonances [35]. In the existing literature, stability issues of the grid-tied inverter in CCM mode have been thoroughly investigated, and the stability enhancement methods have been extensively studied [36], [37]. However, the stability study on the *LCL*-type grid-tied inverter with CRM is still insufficient. Addressing this gap, this article contributes a comparative stability analysis between the proposed charge control method and the conventional average current control in grid-tied CRM inverters.

This article draws inspiration from the concept of OCC and proposes a novel charge control scheme for the CRM grid-tied inverter. The outcomes of this article are summarized as follows.

1) This article proposes a novel charge control method for CRM grid-tied inverters. By regulating the total charge in the inverter-side inductor over one control cycle—effectively aggregating variable switching-cycle charges—it enables constant-frequency control despite time-varying switching frequencies, ensuring reliable CRM operation.
2) The proposed charge control incorporates a model-based feedforward mechanism in the control loop, which precisely correlates the accumulated charge in the inverter-side inductor with the turn-ON duration of power switches. This direct charge-to-time mapping ensures rapid dynamic performance.
3) The proposed charge control enables the indirect regulation of the inverter-side current and, thus, reduces the system order from third-order to first-order. Accordingly, the system robustness against grid impedance variations is highly improved.

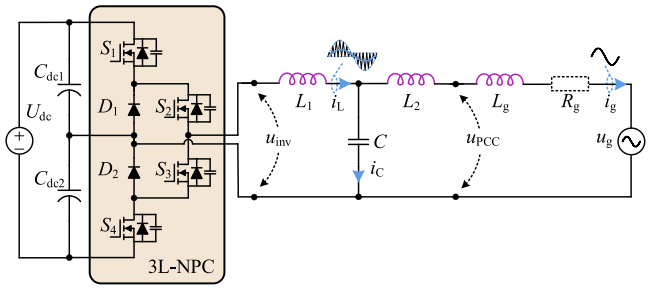

Fig. 1. Circuit structure of the *LCL*-type three-level neutral-point-clamped grid-tied inverter.

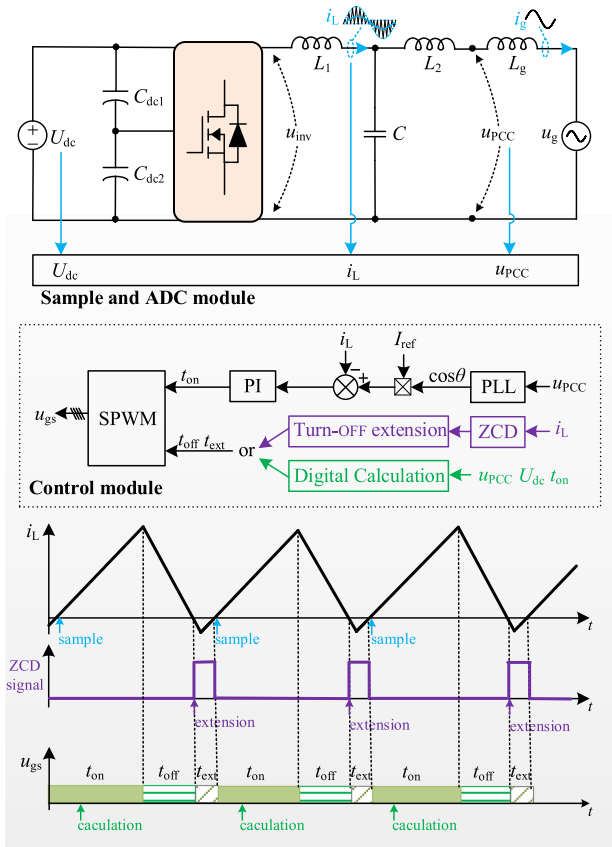

Fig. 2. CRM operation with the average current control.

The rest of this article is organized as follows. Section II presents the system description of the CRM grid-tied inverter. Section III analyzes charge characteristics and proposes the charge control. Section IV develops the system model and conducts a comparative analysis in terms of dynamics and stability performance. In Section V, experimental results are provided to verify the theoretical analysis. Finally, Section VI concludes this article.

II. Review of CRM Grid-Tied Inverters With the Conventional Average Current Control

The *LCL*-type three-level neutral-point-clamped grid-tied inverter is taken as an example in this article. The topology is shown in Fig. 1. The *LCL* filter is composed of the inverter-side

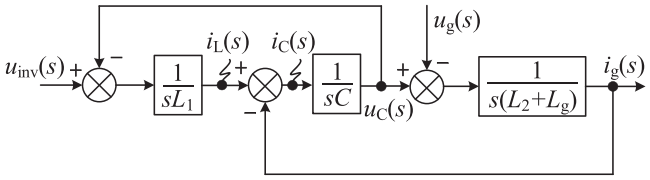

Fig. 3. Simplified model of CRM grid-tied inverter.

inductor L_1, the filter capacitor C, and the grid-side inductor L_2. In Fig. 1, i_L, i_g, and i_C represent the current flowing through L_1, L_g, and C, respectively. C_{dc1} and C_{dc2} are dc-link capacitors. U_{dc} represents the dc-link voltage, u_{inv} represents the voltage between bridge legs, and u_{PCC} represents the PCC voltage. The power grid is equivalent to an ideal voltage source u_g in series with a grid impedance that consists of inductance L_g and resistance R_g [38]. Depending on the grid configuration, the grid impedance may fluctuate in a wide range, leading to the variation of the resonance frequency and further posing a stability risk to grid-tied inverters. Since R_g can provide damping and benefit stability, a pure inductance L_g is considered here to emulate the worst case.

The soft-switching CRM operation with the conventional average current control, as shown in Fig. 2, is briefly illustrated as follows. When the inverter-side current reaches zero, the inverter-side filter inductor and the junction capacitors of the switches resonate. During the resonant period, the drain-to-source voltage of the switch goes down to zero, and thus, the ZVS turn-ON can be achieved.

The soft-switching CRM operation has two typical implementation approaches. One is based on the zero-crossing distortion (ZCD) circuit [39]. The circuit is employed to generate the ZCD signal for synchronous switches, and the turn-OFF extension after the ZCD signal is used to generate the reverse inductor current. The other one is based on the direct digital calculation [40]. It plots the state plane trajectory considering the reverse inductor current, thereby calculating the OFF-time t_{OFF} and the extension-time t_{ext}.

Via the above control scheme, control signals of the switches are generated, and the voltage of the bridge legs, i.e., u_{inv}, can be obtained. As shown in Fig. 1, the grid current i_g is determined by both the bridge legs u_{inv} and the grid voltage u_g. Fig. 3 shows the simplified block diagram of the CRM grid-tied inverter. According to Fig. 3 and the superposition theorem, i_g is expressed as

$$i_g(s) = G_1(s)\,u_{inv}(s) + G_2(s)\,u_g(s) \tag{1}$$

where

$$\begin{cases} G_1(s) = \dfrac{1}{L_1(L_2+L_g)Cs^3+(L_1+L_2+L_g)s} \\ G_2(s) = \dfrac{-\left(L_1Cs^2+1\right)}{L_1(L_2+L_g)Cs^3+(L_1+L_2+L_g)s}. \end{cases} \tag{2}$$

III. Proposed Charge Control for CRM Grid-Tied Inverters

In this section, by analyzing the charge characteristics of the CRM grid-tied inverter, the mathematical relationship between the charge flowing through the inverter-side inductor and the turn-ON time in a switching cycle is identified. The basic principle and implementation of the charge control are presented on its basis.

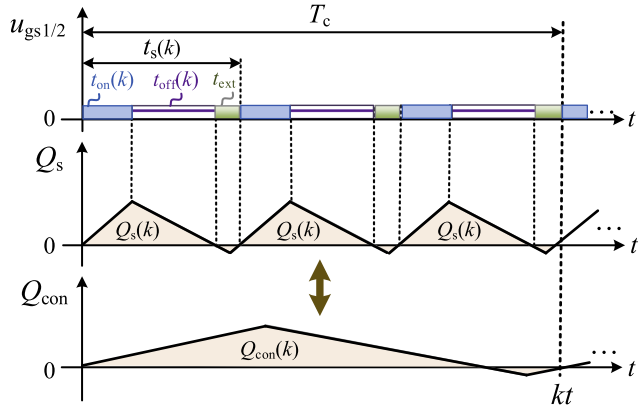

Fig. 4. Charge accumulation in the kth control cycle.

A. Charge Characteristics of the CRM Grid-Tied Inverter

To reduce the computation burden, a fixed control frequency, denoted as f_c, is employed for the CRM grid-tied inverter. Each control cycle contains several switching cycles. Besides, note that f_c is much lower than the grid frequency f_g. Accordingly, during each control cycle, the dc-link voltage U_{dc}, the grid voltage u_g, and the grid current i_g can be regarded to be unchanged, consequently yielding the constant switching period t_s, the turn-ON time t_{ON}, the turn-OFF time t_{OFF}, and the extension time t_{ext} in each control cycle.

Fig. 4 illustrates the charge accumulation in the kth control cycle. $u_{gs1/2}$ represents the gating signals of switches S_1 or S_2. $Q_s(k)$ represents the output charge within the kth control cycle. It can be observed that Q_s are accumulated during the turn-ON interval and decay during the turn-OFF interval. By integrating the total charge over multiple switching cycles, the charge in the kth control cycle can be equivalently represented by $Q_{con}(k)$.

Define the number of switching cycles in the kth control cycle as $n(k)$, i.e.,

$$n(k) = \left\lfloor \frac{Tc}{ts(k)} \right\rfloor \tag{3}$$

where $\lfloor X \rfloor$ indicates the bottom integral of X. T_c represents the constant control cycle. $t_s(k)$ represents the switching cycle in the kth control cycle.

Accordingly, the relationship between $Q_{con}(k)$ and $Q_s(k)$ is expressed as

$$Q_{con}(k) = n(k)Q_s(k). \tag{4}$$

Before calculating $Q_{con}(k)$, the relation of $Q_s(k)$ to the turn-ON time $t_{ON}(k)$ is studied as follows. Zooming in a single switching cycle, the waveform of i_L and the accumulated charge $Q_s(k)$ are given in Fig. 5. As shown, i_L gradually rises during the ON-time t_{ON}, drops during the OFF-time t_{OFF}, and reversely rises

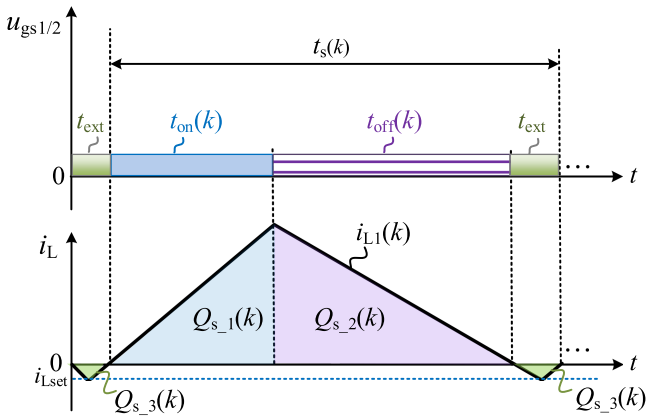

Fig. 5. Waveforms of the inverter-side current i_L, the bridge voltage u_{inv} and accumulated charge $Q_s(k)$.

during the extension-time t_{ext}. According to the trends of i_L, $Q_s(k)$ can be separated into three parts, i.e., $Q_{s\_1}(k)$, $Q_{s\_2}(k)$, and $Q_{s\_3}(k)$, which represent the accumulated or reduced charges of the rising, falling, and reversely rising i_L, respectively.

As shown in Fig. 5, based on the volt-second balance theorem, the relationship between $t_{ON}(k)$ and $t_{OFF}(k)$ during one switching cycle can be expressed as

$$[U_{dc}/2 - u_C(k)]\, t_{on}(k) = u_C(k)\, t_{off}(k). \tag{5}$$

The accumulated charge during the two subintervals $t_{ON}(k)$ and $t_{OFF}(k)$, i.e, $Q_{s\_1}(k)+Q_{s\_2}(k)$, is derived as

$$\begin{aligned} Q_{s\_1}(k) + Q_{s\_2}(k) &= \int_0^{T_c} i_L(t)dt \\ &= \frac{i_{Lp}(k)\,[t_{on}(k) + t_{off}(k)]}{2} \end{aligned} \tag{6}$$

where $i_{Lp}(k)$ is the peak value of i_L and expressed as

$$i_{Lp}(k) = \frac{U_{dc}/2 - u_C(k)}{L_1} t_{on}(k). \tag{7}$$

Subtracting $t_{OFF}(k)$ from (5), and substituting it and (7) into (6), the expression of $Q_{s\_1}(k)+Q_{s\_2}(k)$ is rewritten as

$$Q_{s\_1}(k) + Q_{s\_2}(k) = \frac{U_{dc}\,[U_{dc}/2 - u_C(k)]}{4L_1 u_C(k)} t_{on}^2(k). \tag{8}$$

To ensure that the junction capacitor of the switch can fully resonate with L_1, the reverse reset current, denoted as i_{Lset}, is generally considered as -1A, and the extension-time t_{ext} is set as a resonant period to achieve the ZVS turn-ON [16], i.e.,

$$t_{ext} = T_{ext} = 2\pi\sqrt{L_1 C_{oss}} \tag{9}$$

where C_{oss} is the output capacitance of each switch. Correspondingly, the charge $Q_{s\_3}(k)$ can be calculated as

$$Q_{s\_3}(k) = \frac{2\pi\sqrt{L_1 C_{oss}} \cdot i_{Lset}}{2} = -\pi\sqrt{L_1 C_{oss}}. \tag{10}$$

Therefore, the total charge $Q_s(k)$ during one switching cycle can be given by (11) shown at the bottom of this page. Recalling (4), the charges accumulated during multiple switching cycles of the kth control cycle are equivalently integrated into the total charge $Q_{con}(k)$. Substituting (11) into (4), the integrated charge $Q_{con}(k)$ can be obtained and expressed as (12) shown at the bottom of the this page.

According to (11), the relation of $Q_s(k)$ to the turn-ON time $t_{ON}(k)$ is given by

$$t_{on}(k) = \sqrt{\frac{4L_1 u_C(k)}{U_{dc}\,[U_{dc}/2 - u_C(k)]}\left[Q_s(k) + \pi\sqrt{L_1 C_{oss}}\right]}. \tag{13}$$

As long as (13) is satisfied, the charge $Q_s(k)$ during one switching cycle must satisfy (11), and accordingly, the total charge $Q_{con}(k)$ accumulated during the entire control cycle would be naturally adjusted to satisfy (12). As a result, the full range ZVS turn-ON of switches can be achieved.

B. Basic Principle of Proposed Charge Control

On the basis of the above charge characteristics analysis, the charge control for CRM grid-tied inverters is proposed. Different from the conventional average current control illustrated in Section II, the proposed scheme controls the total charge in the inverter-side inductor per each control cycle.

Fig. 6 illustrates the system block diagram of the *LCL*-type CRM grid-tied inverter with the proposed charge control. The control loop first compares the sampled inverter-side inductor current with its reference, then processes the current error with a PI regulator, yielding the charge reference. The core innovation of the proposed charge control lies in utilizing the model-based feedforward function [i.e., (13)] integrated into the control path. It establishes an accurate mathematical relationship between the inductor's accumulated charge and the required switch turn-ON duration. Thanks to the direct charge-to-time mapping mechanism, the charge control can offer a fast control and excellent dynamic response.

The output of the model-based feedforward function is the turn-ON time $t_{ON}(k)$. The extension-time T_{ext} was expressed as (9). Combining (5) and (7), and considering $u_C \approx u_g$ and $i_{Lp} \approx 2i_{ref}$, the OFF-time $t_{OFF}(k)$ is given by

$$t_{off}(k) = \frac{L_1 i_{Lp}(k)}{u_C(k)} \approx \frac{2L_1 i_{ref}(k)}{u_g(k)}. \tag{14}$$

$$Q_{s\_1}(k) + Q_{s\_2}(k) = \frac{U_{dc}\,[U_{dc}/2 - u_C(k)]}{4L_1 u_C(k)} t_{on}^2(k) - \pi\sqrt{L_1 C_{oss}} \tag{11}$$

$$Q_{con}(k) = \frac{U_{dc}\,[U_{dc}/2 - u_C(k)]\, n(k)}{4L_1 u_C(k)} t_{on}^2(k) - \pi\sqrt{L_1 C_{oss}} \cdot n(k). \tag{12}$$

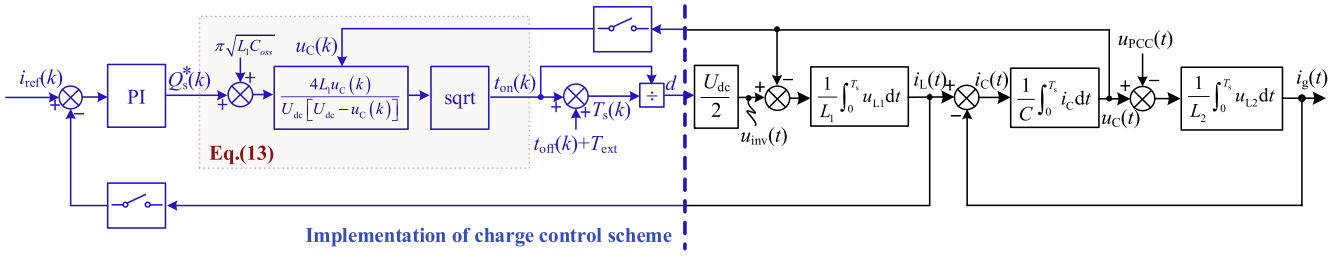

Fig. 6. Block diagram of the *LCL*-type CRM grid-tied inverter with the proposed charge control.

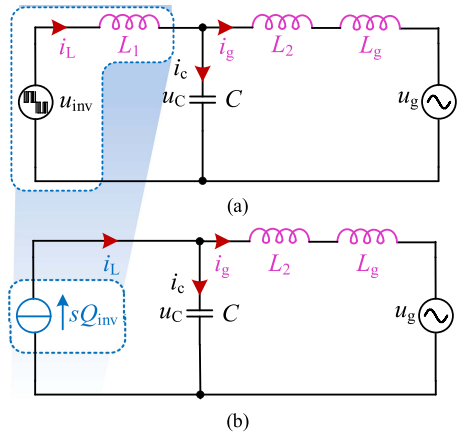

Fig. 7. Physical notations of the *LCL*-type CRM grid-tied inverter. (a) Conventional average current control. (b) Proposed charge control.

By regulating these variables, switching actions are determined.

For better clarity, the physical representation of the *LCL*-type CRM grid-tied inverter with the proposed charge control is illustrated below. As for the grid-tied inverter with the conventional average current control, it can be represented by a controllable voltage source $u_{\rm inv}$ in series with the *LCL* filter, as shown in Fig. 7(a). In contrast, the equivalent circuit with the proposed charge control is represented by a controllable current source $sQ_{\rm inv}$ in series with the *LC* filter, as shown in Fig. 7(b), and the physical interpretations are further provided

Note that the variable controlled by the proposed control is the charge flowing through the inverter-side inductor. Also, the charge flowing out of the bridge leg is denoted as $Q_{\rm inv}$. Since $Q_{\rm inv}$ must flow through L_1, the situation of $Q_{\rm inv} = Q_{\rm L1}$ holds. $Q_{\rm L1}$ and $i_{\rm L}$ have the following integral relationship:

$$i_{\rm L} = sQ_{\rm L1} = sQ_{\rm inv}. \tag{15}$$

Thus, the controllable current source $sQ_{\rm inv}$ is modeled in the circuit notation, and it denotes the reference-to-charge response of the system. Compared with Fig. 7(a), the voltage source $u_{\rm inv}$ and the inverter-side inductor sL_1 are uniformly equivalent to a current source $sQ_{\rm inv}$. Essentially, the proposed charge control is an optimized OCC. By controlling the output charge $Q_{\rm inv}$, the inverter-side current $i_{\rm L}$ is indirectly controlled.

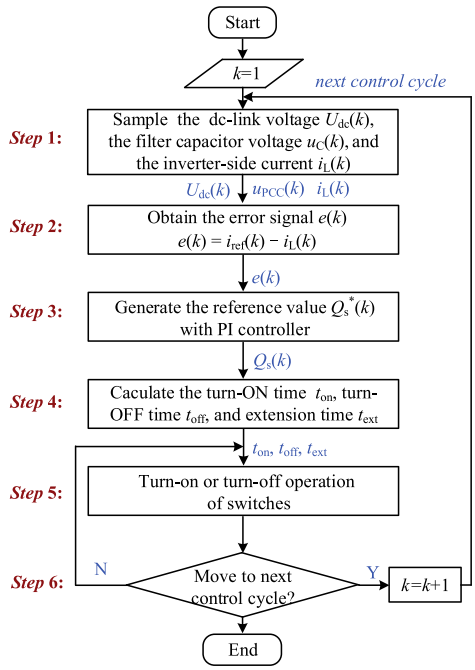

Fig. 8. Flow chart of the proposed charge control.

From Fig. 7(b), the grid current $i_{\rm g}$ is expressed as

$$i_{\rm g}(s) = G_Q(s)\,Q_{\rm inv}(s) + G_{\rm u}(s)\,u_{\rm g}(s) \tag{16}$$

where

$$\begin{cases} G_Q(s) = \dfrac{s}{(L_2+L_g)Cs^2+1} \\ G_{\rm u}(s) = \dfrac{-sC}{(L_2+L_g)Cs^2+1}. \end{cases} \tag{17}$$

Since the inductance sL_1 is involved in the current source $sQ_{\rm inv}$, the order of the equivalent circuit is reduced, as shown in (16) and (17). Thus, the system analysis can be simplified.

C. Implementation of Proposed Charge Control

Based on the above analysis, the flow chart of charge control implementation is depicted in Fig. 8. The control cycle number k is initialized as $k = 1$, and the procedure is elaborated below.

Step 1: The dc-link voltage $U_{\rm dc}$, the filter capacitor voltage $u_{\rm C}$ and the inverter-side current $i_{\rm L}$ are sampled. Notice that the low-pass filter is required to obtain the average current of $i_{\rm L}$ per control cycle (the fundamental component).

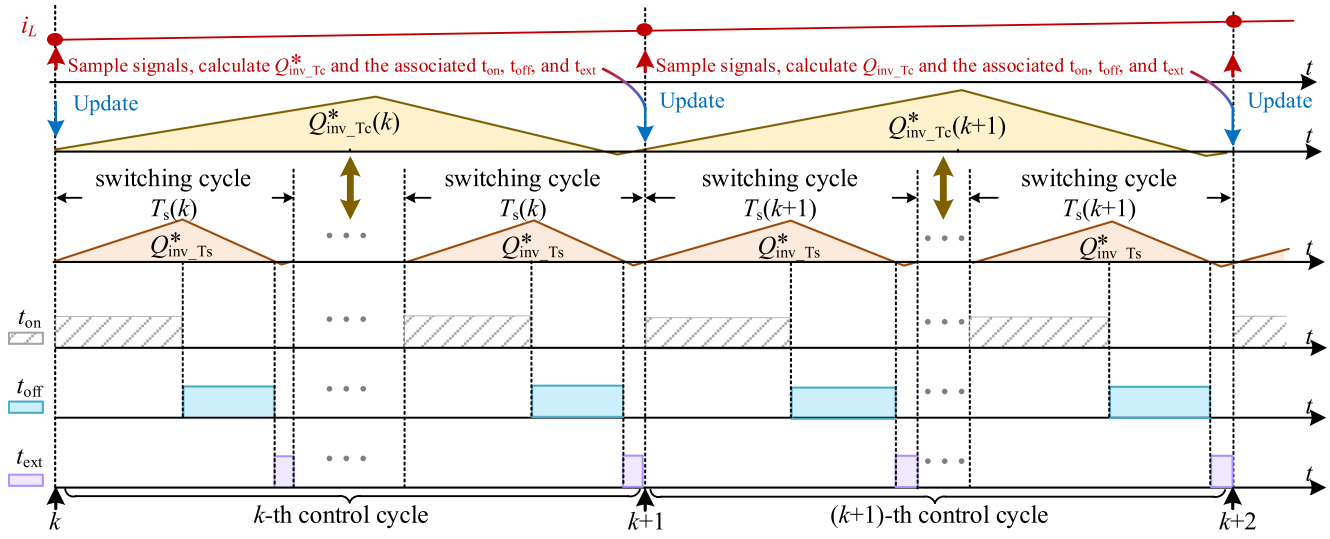

Fig. 9. Pulse sequences of the proposed charge control.

Step 2: Within the kth control cycle, the sampled inverter-side current $i_L(k)$ is compared with the referenced current $i_{ref}(k)$, and the error signal $e(k)$ is obtained.

Step 3: The error signal $e(k)$ is sent to the PI current controller, and its output is the reference value of the charge within one switching cycle, denoted as $Q_s{}^*(k)$.

Step 4: Calculate the turn-ON time $t_{ON}(k)$ according to (13) and set it to the modulator as part of switch gating signals.

Step 5: By applying the turn-ON time $t_{ON}(k)$, the turn-OFF time t_{OFF}, and the extension time t_{ext} to the drive circuit, the total charge output in the kth control cycle is controlled.

Step 6: Check whether the time step moves to the next control cycle. If met, the procedure from *step 1* to *step 6* is repeated. Otherwise, the calculated $t_{ON}(k)$ remains unchanged, and the procedure returns to *step 5*.

For better clarity, the implementation of the charge control is further presented with pulse sequences in the time domain, as shown in Fig. 9.

As can be observed, the turn-ON time t_{ON}, the turn-OFF time t_{OFF}, and the extension time t_{ext} are updated at each control instant and remain constant within the control cycle. Accordingly, the switching frequency in a single control cycle remains fixed, but differs for different control cycles. Therefore, the selection of the fixed digital control frequency is crucial to system performance.

D. Determination of the Digital Control Frequency

Under constant digital control frequency operation, every digital control cycle includes multiple switching periods. Parameters including t_{ON} t_{OFF}, and t_{ext} can only be updated at digital control instants rather than every switching instant. Compared to switching-cycle-level signal updates, approximation errors of t_{ON} t_{OFF}, and t_{ext} exist. Theoretical analysis reveals that higher digital control frequencies reduce power losses caused by approximation errors under constant output power conditions, thereby enhancing system efficiency. However, increasing control frequency imposes greater computational demands on the controller, necessitating a trade-off optimization between control precision and resource allocation.

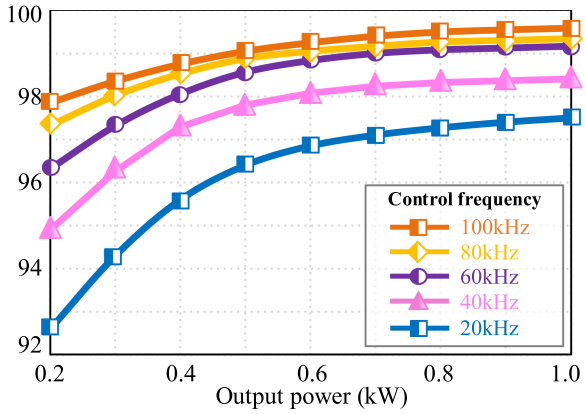

Fig. 10. Efficiency comparison of the proposed charge control scheme with different control frequencies.

Based on the power loss model established in [17], Fig. 10 illustrates efficiency curves of the proposed charge control under different digital control frequencies. The used main parameters are given in Table I in Section V. The curves demonstrate a marked improvement in overall efficiency as the control frequency f_c increases from 20 kHz to 60 kHz. Notably, further increasing f_c beyond 60 kHz, the efficiency improvement becomes insignificant. This is because when a control cycle contains fewer than two switching actions, the benefits of increasing control frequency in error suppression diminishes. Through quantitative analysis of the relationship between control accuracy and computation complexity, $f_c = 60$ kHz is selected for our experimental platform.

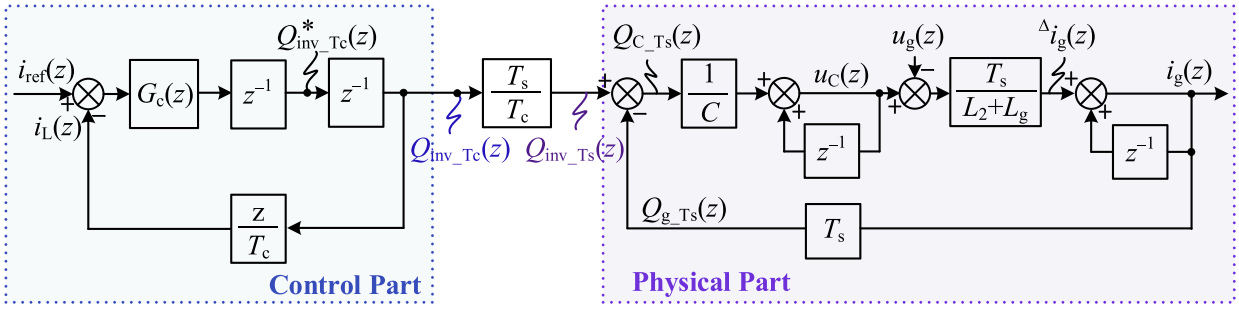

Fig. 11. Discrete-domain block diagram of the CRM grid-tied inverter with charge control.

TABLE I
PARAMETERS OF THE EXPERIMENTAL PROTOTYPE

Parameter	Value
Dc-link (U_{dc})	500 V
Transformer ratio	1:2
Primary side voltage (u'_{PCC})	110 V / 50 Hz
Secondary side voltage (u_{PCC})	220 V / 50 Hz
L_1 / C_f / L_2	40 μH / 6.6 μF / 10 μH
Leakage inductor of transformer L_T	200 μH
Rated Power	1 kW
Parameters of PI controller (k_p/k_i)	0.074 / 0.11
Control frequency (f_c)	60 kHz
Switching frequency (f_{sw})	100 kHz–300 kHz

IV. Discrete-Domain Model and Performance Analysis of the CRM Grid-Tied Inverter With Charge Control

The discrete-domain model of the CRM inverter with the charge control is developed and on its basis, the system performance is studied.

A. Discrete-Domain Modelling

The time-domain model shown in Fig. 6 is highly nonlinear and contains time-varying terms. Although it is accurate and reflects the control responses at any instants, this model is not convenient for studying the system performance. Since the essence of the proposed charge control is to regulate the total charge of the inverter-side current in each fixed control cycle, i.e., Q_{inv_Tc}, we take Q_{inv_Tc} as the intermediate variable linking the control part and physical part, and establish the discrete-domain control model. For better clarity, the mathematical modeling of the physical part and the control part are subsequently elaborated as follows.

1) *Modeling of the Control Part*

As shown in Fig. 9, at time step k, signals such as the inverter-side current i_L are sampled and sent to the current regulator G_c, yielding the charge reference and the associated turn-ON time t_{ON}, turn-OFF time t_{OFF}, and extension time t_{ext}. In order to avoid the unwanted intermediate pulse transitions, the calculated results are not updated until the time step $(k+1)$. Thus, the one-sample computation delay of T_c is introduced into the control loop, which is denoted as z^{-1} in discrete domain.

Through multiple switching actions in the whole control cycle, the expected charge $Q*_{inv\_Tc}(k)$ uploaded at the time step k will be achieved at the time step $k+1$. This process from $Q*_{inv\_Tc}(k)$ to $Q_{inv\_Tc}(k)$ brings another one-sample computation delay z^{-1}.

Furthermore, considering that the sampled inverter-side current at the time step $(k+1)$ can be approximately represented by $i_L(k+1) \approx Q_{inv\_Tc}(k)/T_c$, the feedback of i_L can be presented by the feedback of Q_{inv_Tc} with the gain of z/T_c.

Based on the above analysis, the control part of the system is depicted, as shown in Fig. 11. According to Fig. 11, the transfer function from $i_{ref}(z)$ to $Q_{inv\_Tc}(z)$ in the control part, denoted as $G_{con}(z)$, can be expressed as

$$G_{con}(z) = \frac{G_c(z) \cdot z^{-2}}{1 + G_c(z) \cdot z^{-1}/T_c}. \tag{18}$$

By performing the forward Euler method to the PI controller, $G_c(z)$ is expressed by

$$G_c(z) = k_p + k_i \frac{T_c}{z-1}. \tag{19}$$

2) *Modeling of the Physical Part*

Note that each control cycle consists of multiple switching periods. The proposed charge control evenly distributes the charge reference of a control cycle into multiple switching-period charge references, thereby determining the turn-ON and turn-OFF times of the switching devices. This enables charge regulation through high-frequency switching actions. In each switching period, the charge flowing through L_1 is $Q_{inv\_Ts} = (T_s/T_c)Q_{inv\_Tc}$.

According to the charge conservation principle, the charge leaving L_1 in each switching period equals the sum of the charges flowing into C and L_2+L_g, i.e.,

$$\begin{aligned} Q_{inv\_Ts}(k) &= Q_{C\_Ts}(k) + Q_{g\_Ts}(k) \\ &= C[u_C(k) - u_C(k-1)] + i_g(k) T_s \end{aligned} \tag{20}$$

where $u_C(k)$ is the capacitor voltage in each switching period, equaling the sum of the grid voltage and the voltage across the

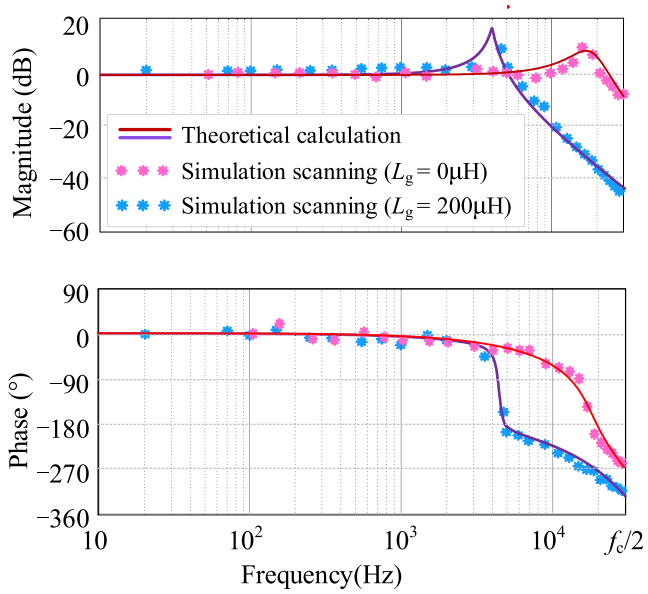

Fig. 12. Frequency response curves of the theoretical model and the simulation frequency-scanning measurement under different L_g.

grid-side inductor, expressed as

$$u_C(k) = u_g(k) + u_{L2}(k) + u_{Lg}(k) = u_g(k) + (L_2 + L_g)\frac{i_g(k) - i_g(k-1)}{T_s}. \quad (21)$$

Thus, the z-domain model of the physical system can be obtained, as shown in Fig. 11. According to Fig. 11, the transfer function from $Q_{inv\_Ts}(z)$ to $i_g(z)$ in the physical part, denoted as $G_{phy}(z)$, can be expressed as

$$G_{phy}(z) = \frac{T_s}{(L_2 + L_g)C(1 - z^{-1})^2 + T_s^2}. \quad (22)$$

It is worth noting that the discretization of the control part is performed at the control cycle T_c whereas the physical part is discretized at the switching period T_s.

Different with the time-domain model in Figs. 6 and 9 employs the accumulated total charge in each control cycle as intermediate variable, which makes the model simple. These two models in essence are equivalent.

According to Fig. 9, define $\Phi(z)$ as the transfer function from $i_{ref}(z)$ to $i_g(z)$, which is expressed as

$$\Phi(z) = \frac{T_s}{T_c} G_{con}(z) G_{phy}(z) \quad (23)$$

and the output admittance of the CRM inverter with the charge control, denoted as $Y_{cha}(z)$, can be derived as

$$Y(z) = \frac{T_s(L_2 + L_g)(1 - z^{-1})}{(L_2 + L_g)C \cdot (1 - z^{-1})^2 + T_s^2}. \quad (24)$$

With the main parameters listed in Table I, the closed-loop frequency response curves of the CRM grid-tied inverter with the proposed charge control under grid conditions of $L_g = 0$ μH and $L_g = 200$ μH are depicted, as shown by the solid lines in Fig. 12. To verify the accuracy of the developed model,

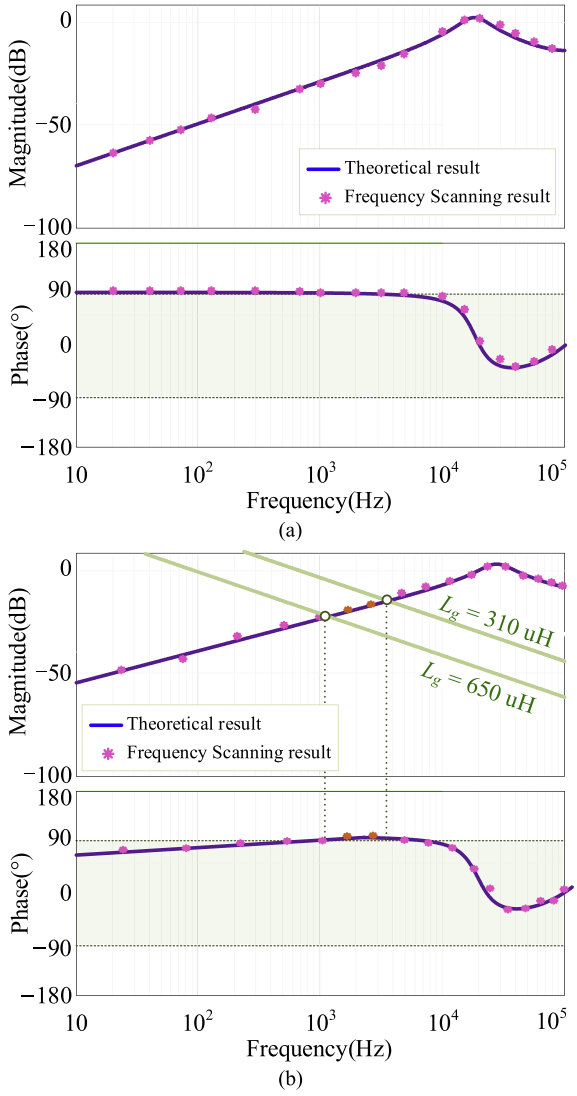

Fig. 13. Output admittance of the CRM inverter with (a) the charge control and (b) the average current control.

the simulation model is built in MATLAB Simulink and the frequency-sweeping measurements are also provided, as shown by the dotted lines in Fig. 12. It can be observed that the theoretical model matches well with the measurement, which confirms that the developed model is accurate.

B. System Performance

The system performance is compared with the average current control based on the developed discrete domain model. To ensure the fairness of the comparison, these two control methods are evaluated under identical main parameters and PI controller parameters. According to [41], the PI parameters are designed to achieve PM in the range of (30°, 60°) and GM≥ 3−6 dB to ensure both a good dynamic response and robust stability. The parameters are listed in Table I.

In principle, the proposed charge control embeds a model-based feedforward function in the control path, to directly

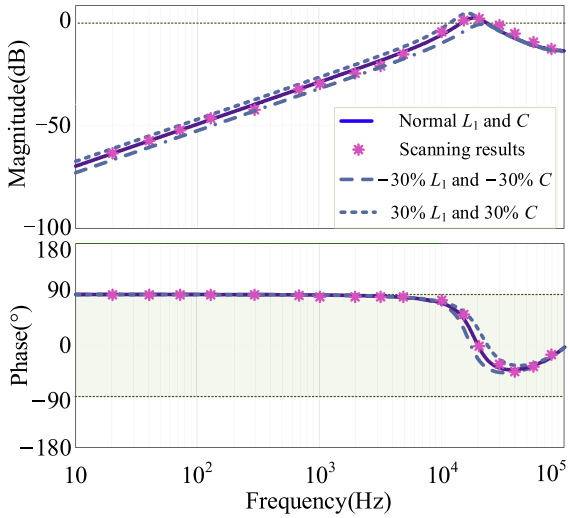

Fig. 14. Output admittance of the CRM grid-tied inverter with the charge control considering the filter parameter fluctuations.

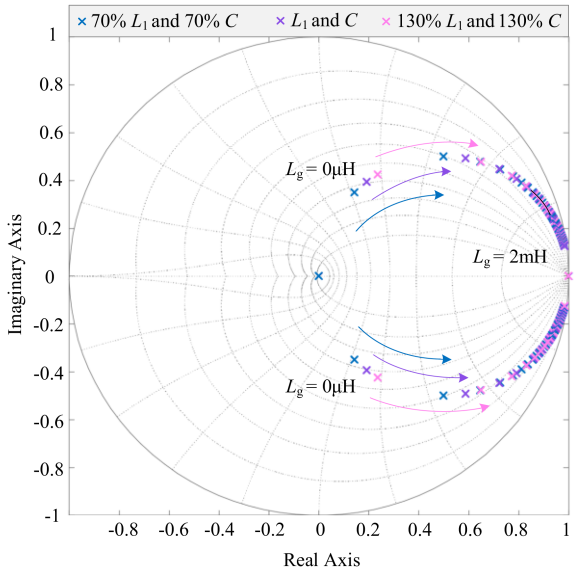

Fig. 15. Closed-loop pole maps with the charge control under filter parameter variations.

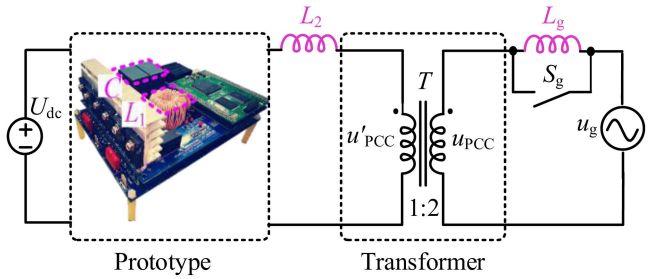

Fig. 16. Experimental platform of the *LCL*-type CRM grid-tied inverter.

establish the regulatory relationship between the charge flowing through the inverter-side inductor and the turn-ON time of switches. As a result, it provides fast regulation and excellent dynamic response.

As mentioned, depending on the grid configuration, the grid admittance may vary with a wide range. To better evaluate the system robustness against the grid impedance, the inverter output admittance of the charge control and the average current control are plotted in Fig. 13(a) and (b), respectively. The solid lines and dotted lines represent the theoretical results and frequency-scanning measurements, respectively. As shown in Fig. 13(a), the phases of the output admittance with the charge control stay within the range of (−90°, 90°), implying that the corresponding output admittance is passive; In contrast, there exists the non-passive frequency region for the output admittance with the average current control, as shown in Fig. 13(b). According to the impedance-based stability criterion, when the intersection frequency of output admittance and grid admittance in the magnitude plots falls into the nonpassive region, the system may be unstable. Thus, the proposed charge control endows the system with a strong robustness.

Furthermore, the system sensitivity to filter parameter fluctuations is also evaluated. Considering the fluctuations of $\pm 30\% L_1$ and $\pm 30\% C$, the output admittance and closed-loop poles map with the charge control are plotted, as shown in Figs. 14 and 15, respectively. As can be observed from Fig. 15, the output admittance with the charge control is always passive. As can be observed from Fig. 16, the poles are always located in the unit circle when L_g varies from 0 μH up to 2 mH. These results prove that the system has strong adaptability to the filter parameter fluctuation.

In summary, compared with the conventional average current control, the proposed charge control has stronger stability, better dynamic response, and superior adaptability to the variations in grid impedance and filter parameters, making it more attractive for the *LCL*-type CRM grid-tied inverters.

V. Experimental Verification

A 1-kW CRM grid-tied inverter prototype with parameters listed in Table I was built for experimental verification. The half-bridge neutral-point-clamped circuit topology is adopted, and the platform is shown in Fig. 16. Note that the leakage inductor of transformer L_T is regarded as part of the grid impedance L_g. The control algorithm is implemented in the DSP TMS320F28377S, the dc voltage is provided by the Itech dc source IT6012B-800-40, and the power grid is emulated by the programmable ac-source Chroma 61512. To demonstrate advantages of the proposed charge control method, comparative experimental studies were performed against the conventional fully-digital average current control approach [17], using identical control frequency. Both control schemes were tested with the CRM inverter operating at switching frequencies ranging from 100 kHz to 300 kHz, while maintaining a fixed control frequency of 60 kHz for fair comparison.

The first set of experiments was carried out to examine the steady-state performance. The corresponding waveforms with the proposed charge control scheme and the average current control scheme are shown in Fig. 17(a) and (b), respectively. The quality of the grid current i_g exhibits good sinuosity while using either the proposed charge control scheme or the average

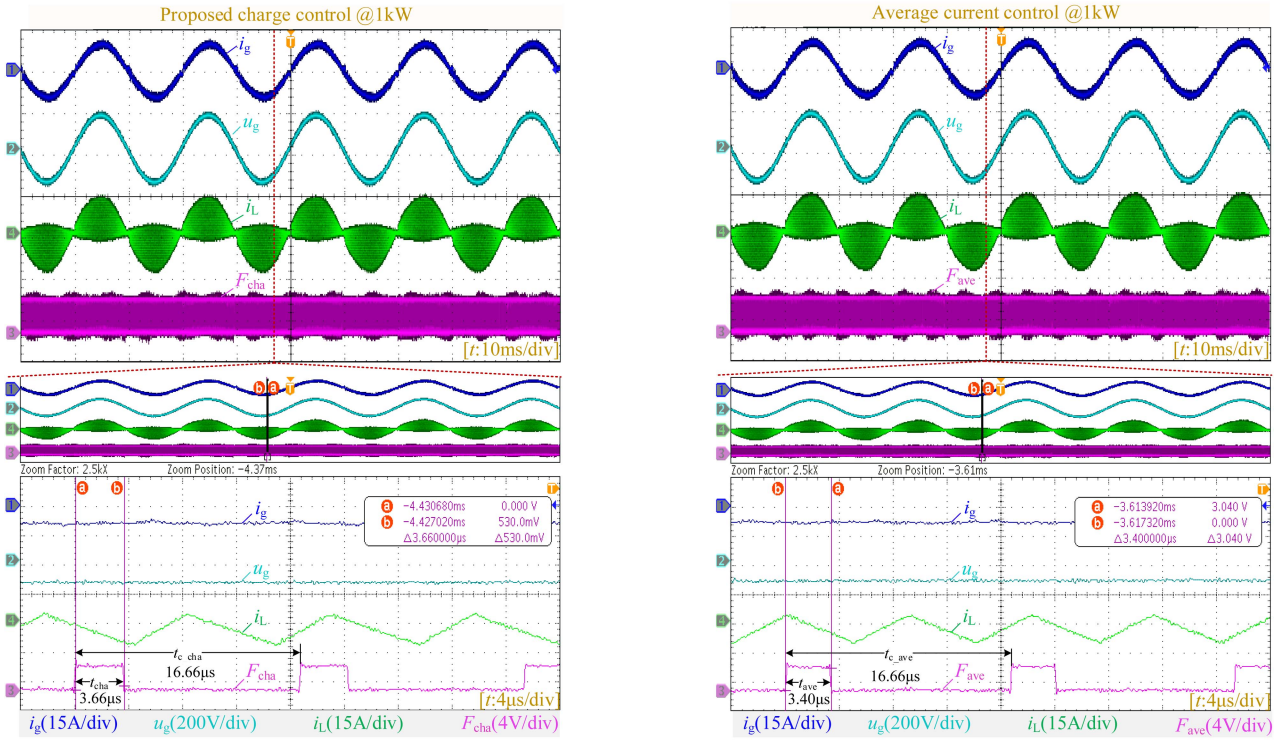

Fig. 17. Steady-state waveforms of the CRM grid-tied inverter with. (a) Proposed charge control scheme. (b) Average current control scheme.

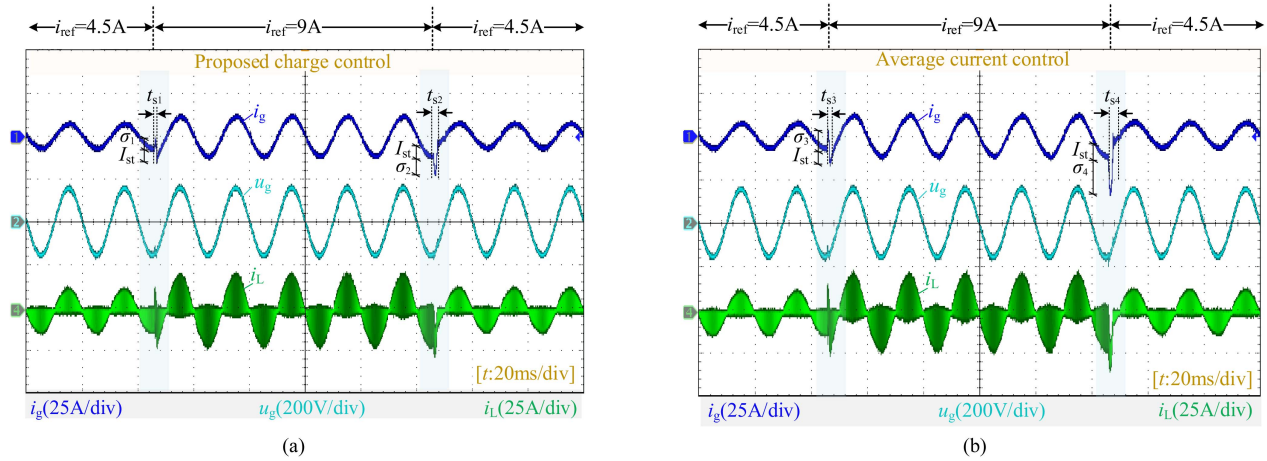

Fig. 18. Dynamic waveforms of the CRM grid-tied inverter when the current reference changes between half- and full-load. (a) Proposed charge control scheme. (b) Average current control scheme.

current control scheme. The measured total harmonic distortions of i_g with the charge control and the average current control is only 2.3% and 2.2%, respectively. The above results confirm that the proposed charge control is effective in ensuring high-quality grid currents injected into the power grid. Besides, the interrupt signals ($F_{\rm cha}$ and $F_{\rm ave}$) marking the control calculation cycles are also presented in Fig. 17, with the zoomed-in view explicitly revealing their program execution times. It can be observed that the program execution time of the proposed charge control scheme and the average current control scheme are 3.66 μs and 3.40 μs, respectively.

The second set of experiments was carried out to examine the dynamic performance. In order to emulate the worst-case scenario, step changes of the current reference occurred at the peak of $u_{\rm PCC}$. For a half-to-full load transition, Fig. 18(a) and (b) presents the experimental results using the proposed charge control and the average current control, respectively. As show in Fig. 18(a), the proposed control achieves a first overshoot ($\rm PO_1$ $= \sigma_1 / I_{\rm st}$) of 59% with a settling time ($t_{\rm s1}$) of 0.92 ms, and a second overshoot ($\rm PO_2$ $= \sigma_2 / I_{\rm st}$) of 96% with a settling time ($t_{\rm s2}$) of 3.88 ms; In contrast, Fig. 18(b) reveals that the average current control yields significantly larger overshoots ($\rm PO_3$ $=$

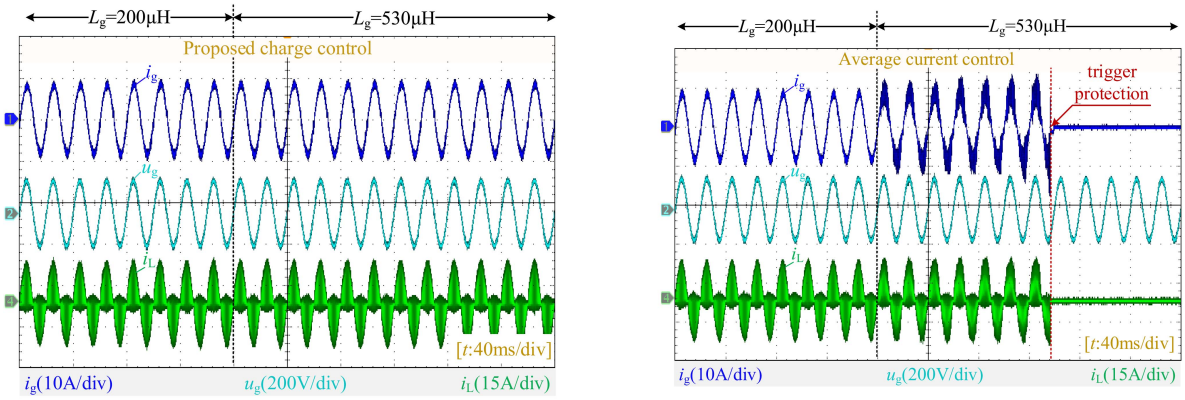

Fig. 19. Stability performances of the CRM grid-tied inverter when the grid impedance alters from $L_g = 200\ \mu$H to $L_g = 530\ \mu$H. (a) Proposed charge control scheme. (b) Average current control scheme.

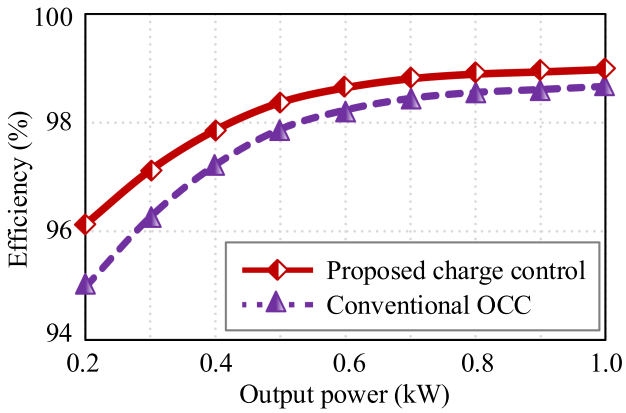

Fig. 20. Efficiency comparison of the conventional OCC with $f_{sw} = 60$ kHz and the charge control with variable f_{sw}.

173%, $PO_4 = 190\%$), and longer settling time ($t_{s3} = 1.23$ ms and $t_{s4} = 4.7$ ms). These results demonstrate that the proposed charge control effectively reduces both percentage overshoot (PO) and settling time, confirming its superior dynamic performance in grid-tied inverter applications.

The third set of experiments was carried out to examine the system robustness against grid impedance variation. Fig. 19 shows the experimental results under different grid impedances. As for the CRM grid-tied inverter with the proposed charge control scheme, as shown in Fig. 19(a), a satisfactory and stable operation is retained when the grid impedance L_g alters from 200 μH to 530 μH. However, as for the CRM grid-tied inverter with the average current control, as shown in Fig. 19(b), oscillation occurs and triggers protection when the grid impedance alters to 530 μH. The results are consistent with the analysis in Section IV, confirming that the superior system robustness of the CRM grid-tied inverter is achieved with the proposed charge control.

The above results demonstrate that, despite comparable program execution time, the proposed method charge control enhances dynamics and robustness of the CRM inverter.

Finally, note that the proposed charge control draws inspiration from the OCC principle and overcomes its limitation of reliance on fixed switching cycles, thereby enabling application to CRM grid-tied inverters with time-varying switching frequencies. Compared to the CCM inverter using conventional OCC scheme, the CRM inverter with the proposed charge control method achieves ZVS and, thus, has higher efficiency. The efficiency comparison curves of the conventional OCC with a fixed switching frequency of 60 kHz and the charge control with variable switching frequency are shown in Fig. 20. It can be observed that the proposed charge control achieves an efficiency improvement of over 0.5%.

VI. Conclusion

This article proposes the charge control scheme for *LCL*-type CRM soft-switching grid-tied inverters. Theoretical analysis and experimental results demonstrate the following characteristics.

1) The proposed charge control is practical and straightforward to implement, which maintains satisfactory control performance with reduced computation burden.
2) The proposed charge control reduces the inverter system order, improving the system robustness against grid impedance variations and facilitating the system analysis.
3) Compared with the conventional average current control scheme, the proposed charge control scheme endows the CRM grid-tied inverter with better dynamics and stronger robustness.

In future research, the proposed charge control scheme will be further extended to the three-phase grid-tied inverter, and its effectiveness will be assessed when integrated with other CRM controls.

References

[1] M. A. Rezaei, K.-J. Lee, and A. Q. Huang, "A high-efficiency flyback micro-inverter with a new adaptive snubber for photovoltaic applications," *IEEE Trans. Power Electron.*, vol. 31, no. 1, pp. 318–327, Jan. 2016.

[2] Y. Shen, M. D'Antonio, S. Chakraborty, A. Hasnain, and A. Khaligh, "Comparison of CCM- and CRM-based boost parallel active power decoupler for PV microinverter," *IEEE Trans. Power Electron.*, vol. 37, no. 8, pp. 9889–9906, Aug. 2022.

[3] L. Zhu, H. Bai, A. Brown, and M. McAmmond, "Transient analysis when applying GaN + Si hybrid switching modules to a zero-voltage-switching EV onboard charger," *IEEE Trans. Transp. Electrific.*, vol. 6, no. 1, pp. 146–157, Mar. 2020.

[4] X. Chen, G. Son, Z. Huang, F. Jin, and Q. Li, "High frequency three-phase CRM inverter with integrated magnetics for auxiliary power supply in railway applications," in *Proc. IEEE Energy Convers. Congr. Expo.*, 2024, pp. 3320–3325.

[5] Z. Wang, Y. Wu, M. H. Mahmud, Z. Zhao, Y. Zhao, and H. A. Mantooth, "Design and validation of a 250-kW all-silicon carbide high-density three level T-type inverter," *IEEE J. Emerg. Sel. Topics Power Electron.*, vol. 8, no. 1, pp. 578–588, Mar. 2020.

[6] M. Stecca, C. Tan, J. Xu, T. B. Soeiro, P. Bauer, and P. Palensky, "Hybrid Si/SiC switch modulation with minimum SiC MOSFET conduction in grid connected voltage source converters," *IEEE Emerg. Sel. Topics Power Electron.*, vol. 10, no. 4, pp. 4275–4289, Aug. 2022.

[7] A. Allca-Pekarovic et al., "Loss modeling and testing of 800-V DC bus IGBT and SiC traction inverter modules," *IEEE Trans. Transp. Electrific.*, vol. 10, no. 2, pp. 2923–2935, Jun. 2024.

[8] C. Liu et al., "Hybrid SiC-Si DC–AC topology: SHEPWM Si-IGBT master unit handling high power integrated with partial-power SiC-MOSFET slave unit improving performance," *IEEE Trans. Power Electron.*, vol. 37, no. 3, pp. 3085–3098, Mar. 2022.

[9] Y. Yan, H. Gui, and H. Bai, "Complete ZVS analysis in dual active bridge," *IEEE Trans. Power Electron.*, vol. 36, no. 2, pp. 1247–1252, Feb. 2021.

[10] J. Hu et al., "Fixed switching frequency hybrid modulation with ZVS for single-phase inverter," *IEEE Trans. Power Electron.*, vol. 38, no. 3, pp. 3114–3126, Mar. 2023.

[11] J. Chen, J. Deng, L. Ming, Z. Xin, W. Yin, and P. Wang, "A variable switching frequency control for ZVS three-phase three-level T-type inverter using hybrid discontinuous PWM," *IEEE Trans. Power Electron.*, vol. 38, no. 11, pp. 13456–13466, Nov. 2023.

[12] J. Deng, C. Hu, K. Shi, M. Chen, and D. Xu, "A ZVS-PWM scheme for three-phase active-clamping T-type inverters," *IEEE Trans. Power Electron.*, vol. 38, no. 3, pp. 3951–3964, Mar. 2023.

[13] T. Liu, C. Chen, K. Xu, Y. Zhang, and Y. Kang, "GaN-based megahertz single-phase inverter with a hybrid TCM control method for high efficiency and high-power density," *IEEE Trans. Power Electron.*, vol. 36, no. 6, pp. 6797–6813, Jun. 2021.

[14] A. Jaquan Dancy, J. Li, and D. Sam Ha, "Split-capacitor boost converter operating in boundary conduction mode with impedance matching for kinetic energy harvesting," in *Proc. IEEE 63rd Int. Midwest Symp. Circuits Syst.*, 2020, pp. 203–207.

[15] G. Son, Z. Huang, Q. Li, and F. C. Lee, "Critical conduction mode based high frequency single-phase transformerless PV inverter," in *Proc. IEEE Appl. Power Electron. Conf. Expo.*, 2020, pp. 3232–3237.

[16] G. Son, Z. Huang, Q. Li, and F. C. Lee, "Analysis and control of critical conduction mode high-frequency single-phase transformerless PV inverter," *IEEE Trans. Power Electron.*, vol. 36, no. 11, pp. 13188–13199, Nov. 2021.

[17] Z. Zheng, L. Zhang, C. Wu, Y. Wang, Z. Lei, and K. Sun, "Variable OFF-time and deadtime scheme with optimized control frequency for soft-switching single-phase inverters," *IEEE Trans. Power Electron.*, vol. 38, no. 4, pp. 4972–4987, Apr. 2023.

[18] Z. Zhang, J. Zhang, S. Shao, and J. Zhang, "A high-efficiency single-phase T-type BCM microinverter," *IEEE Trans. Power Electron.*, vol. 34, no. 1, pp. 984–995, Jan. 2019.

[19] S. Bagawade, M. Pahlevani, and P. Jain, "Novel soft-switched three-phase inverter with output current ripple cancellation," *IEEE Trans. Power Electron.*, vol. 38, no. 1, pp. 1232–1248, Jan. 2023.

[20] C. R. Baier, R. O. Ramirez, E. I. Marciel, J. C. Hernández, P. E. Melín, and E. E. Espinosa, "FCS-MPC without steady-State error applied to a grid-connected cascaded H-bridge multilevel inverter," *IEEE Trans. Power Electron.*, vol. 36, no. 10, pp. 11785–11799, Oct. 2021.

[21] S. Xu, C. Yao, G. Ren, Z. Sun, S. Wu, and G. Ma, "Weighting factors autotuning of FCS-MPC for hybrid ANPC inverter in PMSM drives based on deep residual networks," *IEEE Trans. Power Electron.*, vol. 39, no. 12, pp. 16540–16552, Dec. 2024.

[22] Y. Wang, F. Liu, S. Chen, G. Shen, and Q.-G. Wang, "Prediction errors analysis and correction on FCS-MPC for the Cascaded H-bridge multilevel inverter," *IEEE Trans. Ind. Electron.*, vol. 69, no. 8, pp. 8264–8273, Aug. 2022.

[23] A. R. Nair, R. Bhattarai, M. Smith, and S. Kamalasadan, "A hybrid adaptive control architecture for grid-connected inverter with optimal policy generation," *IEEE Trans. Ind. Electron.*, vol. 58, no. 1, pp. 855–867, Jan./Feb. 2022.

[24] R. M. Milasi, "A nonlinear adaptive control for a bidirectional DC–AC converter with parameter uncertainties," *IEEE Trans. Ind. Electron.*, vol. 71, no. 8, pp. 9551–9558, Aug. 2024.

[25] H. Safamehr, T. A. Najafabadi, and F. R. Salmasi, "Adaptive control of grid-connected inverters with nonlinear LC filters," *IEEE Trans. Power Electron.*, vol. 38, no. 2, pp. 1562–1570, Feb. 2023.

[26] W. Liu and H. Zhang, "Cycle skipping-induced bifurcation analysis of single-inductor bipolar-output DC–DC converters with one-cycle control," *IEEE Trans. Circuits Syst. II, Exp. Briefs*, vol. 70, no. 8, pp. 3134–3138, Aug. 2023.

[27] G. D. S. Fischer, C. Rech, and Y. R. de Novaes, "Extensions of leading-edge modulated one-cycle control for totem-pole bridgeless rectifiers," *IEEE Trans. Power Electron.*, vol. 35, no. 5, pp. 5447–5460, May 2020.

[28] C. Wang, H. Hu, H. Cheng, Z. Zhao, and J. Liu, "Voltage balancing control of cascaded single-phase VIENNA converter based on one cycle control with unbalanced loads," *IEEE Access*, vol. 8, pp. 95126–95136, 2020.

[29] Y. L. Guo, Q. H. Wu, L. Wang, and G. F. Tang, "Stability enhancement of one-cycle controlled buck-boost converters with a composite function embedded," *IEEE Trans. Circuits Syst. I, Reg. Papers*, vol. 67, no. 10, pp. 3512–3520, Oct. 2020.

[30] G. Zhang et al., "Enhanced one-cycle control for multicell power converters," *IEEE Trans. Power Electron.*, vol. 35, no. 8, pp. 8846–8856, Aug. 2020.

[31] Y. Tang, C. Zhang, Y. Guo, H. Sun, and L. Jiang, "Optimization of zero-crossing distortion for unipolar BCM grid-tied inverter," *IEEE Emerg. Sel. Topics Power Electron.*, vol. 11, no. 4, pp. 3680–3691, Aug. 2023.

[32] M. Zhao, J. Chen, Z. Xin, and H. Liu, "A hybrid DPWM based variable switching frequency scheme for ZVS three-phase three-level neutral-point-clamped inverter," *IEEE Trans. Ind. Electron.*, vol. 71, no. 11, pp. 14276–14286, Nov. 2024.

[33] J. Zhao, C. Xie, K. Li, J. Zou, and J. M. Guerrero, "Passivity-oriented design of LCL-type grid-connected inverters with Luenberger observer-based active damping," *IEEE Trans. Power Electron.*, vol. 37, no. 3, pp. 2625–2635, Mar. 2022.

[34] N. N. Nam, N.-D. Nguyen, and Y. I. Lee, "Model predictive control for a voltage sensorless grid-connected inverter with LCL filter using lumped disturbance observer," *IEEE J. Emerg. Sel. Topics Power Electron.*, vol. 11, no. 3, pp. 3050–3063, Jun. 2023.

[35] D. Pan, X. Ruan, C. Bao, W. Li, and X. Wang, "Capacitor-current-feedback active damping with reduced computation delay for improving robustness of LCL-type grid-connected inverter," *IEEE Trans. Power Electron.*, vol. 29, no. 7, pp. 3414–3427, Jul. 2014.

[36] J. Lei, Z. Qin, W. Li, P. Bauer, and X. He, "Stability region exploring of shunt active power filters based on output admittance modeling," *IEEE Trans. Ind. Electron.*, vol. 68, no. 12, pp. 11696–11706, Dec. 2021.

[37] X. Wang and F. Blaabjerg, "Harmonic stability in power electronic based power systems: Concept, modeling, and analysis," *IEEE Trans. Smart Grid*, vol. 10, no. 3, pp. 2858–2870, May 2019.

[38] M. Liserre, R. Teodorescu, and F. Blaabjerg, "Stability of photovoltaic and wind turbine grid-connected inverters for a large set of grid impedance values," *IEEE Trans. Power Electron.*, vol. 21, no. 1, pp. 263–272, Jan. 2006.

[39] Z. Liu, B. Li, F. C. Lee, and Q. Li, "High-efficiency High-density critical mode rectifier/inverter for WBG-device-based on-board charger," *IEEE Trans. Ind. Electron.*, vol. 64, no. 11, pp. 9114–9123, Nov. 2017.

[40] Q. Huang and A. Q. Huang, "Variable frequency average current mode control for ZVS symmetrical dual-buck H-bridge all-GaN inverter," *IEEE Emerg. Sel. Topics Power Electron.*, vol. 8, no. 4, pp. 4416–4427, Dec. 2020.

[41] C. Bao, X. Ruan, X. Wang, W. Li, D. Pan, and K. Weng, "Step-by-Step controller design for LCL-type grid-connected inverter with capacitor–Current-feedback active-damping," *IEEE Trans. Power Electron.*, vol. 29, no. 3, pp. 1239–1253, Mar. 2014.

[42] D. Pan, X. Ruan, X. Wang, H. Yu, and Z. Xing, "Analysis and design of current control schemes for LCL-type grid-connected inverter based on a general mathematical model," *IEEE Trans. Power Electron.*, vol. 32, no. 6, pp. 4395–4410, Jun. 2017.

Yuying He (Member, IEEE) received the B.S. degree in electrical engineering from Central South University, Changsha, China, in 2015, and the Ph.D. degree in electrical engineering from Huazhong University of Science and Technology, Wuhan, China, in 2022.

From 2021 to 2022, she was also with E. ON Energy Research Center, RWTH Aachen University, Aachen, Germany. Since 2022, she has been with Hohai University, Nanjing, China, and she is currently a tenure-track Associate Professor. Her research interests include modeling and control of grid-connected converters, harmonics analysis and control, and stability of renewable energy generation system.

Li Zhang (Senior Member, IEEE) received the B.E. and Ph.D. degrees in electrical engineering from Nanjing University of Aeronautics and Astronautics (NUAA), Nanjing, China, in 2007 and 2012, respectively.

He was with the Faculty of Electrical Engineering, Hohai University, Nanjing, China, in 2014, where he is currently a Professor. From 2012 to 2014, he was a Postdoctoral Research Fellow with the Department of Electrical Engineering, Tsinghua University, Beijing, China. From July to August 2012, he was a Visiting Scholar of Electrical Engineering with the Department of Energy Technology, Aalborg University, Denmark. From 2016 to 2017, he was a Visiting Scholar of Electrical Engineering with the Department of Electrical and Computer Engineering, Ryerson University, Canada. He has authored and coauthored more than 150 peer-reviewed papers published in journals and conference proceedings. He is the holder of more than 50 patents. His current research interests include high-performance power converters and distributed generation technology.

Dr. Zhang is the recipient of the Outstanding Reviewer Award of IEEE TRANSACTIONS ON POWER ELECTRONICS in 2014 and 2020, and IEEE PES Nanjing Chapter Outstanding Young Engineer Award in 2019. He is a member of the Technical Committee on High Performance and Emerging Technologies of IEEE Power Electronics Society. He is currently an Associate Editor for IEEE TRANSACTIONS ON POWER ELECTRONICS.

Zhengzi Lei (Student Member, IEEE) was born in Zhejiang Province, China, in 2000. She received the B.S. and M.S. degrees in electrical engineering from Hohai University, Nanjing, China, in 2022 and 2025, respectively.

Her current research interests include the control of dc–ac converters and the voltage switching in renewable energy generation.

Zhongshu Zheng (Student Member, IEEE) was born in Shandong, China, in 1996. He received the Ph.D. degree in electrical engineering from Hohai University, Nanjing, China, in 2024.

Dr. Zheng was the recipient of the Best Presentation Award of the International Power Electronics and Application Symposium (PEAS) in 2021, and the Best Paper Award of the PEAS in 2023.

Wenbo An (Student Member, IEEE) was born in Shanxi, China, in 2000. He received the B.S. degree in electrical engineering from Hangzhou Dianzi University, Hangzhou, China, in 2023, where he is currently working toward the Ph.D. degree in electrical engineering with Hohai University, Nanjing, China.

His main research interests include high-power-density ac/dc converters and renewable energy generation technologies.